

# RSC Advances



This is an *Accepted Manuscript*, which has been through the Royal Society of Chemistry peer review process and has been accepted for publication.

*Accepted Manuscripts* are published online shortly after acceptance, before technical editing, formatting and proof reading. Using this free service, authors can make their results available to the community, in citable form, before we publish the edited article. This *Accepted Manuscript* will be replaced by the edited, formatted and paginated article as soon as this is available.

You can find more information about *Accepted Manuscripts* in the [Information for Authors](#).

Please note that technical editing may introduce minor changes to the text and/or graphics, which may alter content. The journal's standard [Terms & Conditions](#) and the [Ethical guidelines](#) still apply. In no event shall the Royal Society of Chemistry be held responsible for any errors or omissions in this *Accepted Manuscript* or any consequences arising from the use of any information it contains.

## Comparative evaluation by scanning confocal Raman spectroscopy and transmission electron microscopy of therapeutic effects of noble metal nanoparticles in experimental acute inflammation

Adriana Filip<sup>a##</sup>, Monica Potara<sup>b\*</sup>, Adrian Florea<sup>c</sup>, Ioana Baldea<sup>a</sup>, Diana Olteanu<sup>a</sup>, Pompei Bolfa<sup>d</sup>, Simona Clichici<sup>a</sup>, Luminita David<sup>e</sup>, Bianca Moldovan<sup>e</sup>, Liliana Olenic<sup>f</sup>, Simion Astilean<sup>b</sup>

<sup>a</sup>Department of Physiology, „Iuliu Hatieganu” University of Medicine and Pharmacy, Cluj-Napoca, Romania

<sup>b</sup>Faculty of Physics and Interdisciplinary Research Institute in Bio-Nano-Science, Nanobiophotonics and Laser Microspectroscopy Center, Babes-Bolyai University, Cluj-Napoca, Romania

<sup>c</sup>Department of Cell and Molecular Biology, “Iuliu Hatieganu” University of Medicine and Pharmacy, Cluj Napoca, Romania

<sup>d</sup>Department of Biomedical Sciences, Ross University School of Veterinary Medicine Basseterre, St. Kitts, West Indies

<sup>e</sup>Faculty of Chemistry and Chemical Engineering, Babes-Bolyai University, Cluj-Napoca, Romania

<sup>f</sup>National Institute for Research and Development of Isotopic and Molecular Technologies, Cluj-Napoca, Romania

<sup>#</sup>Corresponding author

Adriana G. Filip

Department of Physiology

1-3 Clinicilor Street, Cluj-Napoca, Romania

[gabriela.filip@umfluj.ro](mailto:gabriela.filip@umfluj.ro); [adrianafilip33@yahoo.com](mailto:adrianafilip33@yahoo.com);

Fax: +40-264-597257

Tel: +40-745-268704

\* These authors contributed equally to this work

## Abstract

The finding of appropriate experimental design and analysis methods aiming to gain insight into the mechanisms of efficiency and toxicity of nanomaterials is a major focus in today research in nanomedicine. In this paper, we demonstrate the ability of scanning confocal Raman spectroscopy to emphasize the molecular changes in terms of inflammation resolution after administration of a single dose of metal nanoparticles functionalized with natural extracts, in experimental inflammation. 4 experimental groups of Wistar rats treated with one dose of gold (AuNPs-CM) and silver nanoparticles (AgNPs-CM), respectively *Cornus Mas* (CM) extract and vehicle, before intraplantar injection of 100  $\mu$ l 1% carrageenan and one group, untreated animals, were used. The paw tissues were harvested and used for transmission electron microscopy (TEM) and evaluation of the metal content at 4 and 24 hours after induction of inflammation and, respectively, at 24 hours for performing Raman spectroscopy, histopathology and prostaglandin (PG) E2 levels assessment. TEM revealed varying degrees of alterations of dermo-epidermal junction and capillaries, especially in tissues treated with AgNPs-CM and vehicle, in parallel with increasing of PGE2 levels. Beside ultrastructural changes highlighted by TEM, meaningful information about the molecular changes is provided by multivariate Raman spectral images. Indeed, thorough Raman spectral analysis shows that AuNPs-CM and CM restored the normal composition of unsaturated fatty acids while the specimens treated with AgNPs-CM were dominated by the protein component.

Our results suggest that the Raman spectral analysis has real potential to be used in tandem with standard methods for monitoring the subtle molecular effects induced by nanoparticles administration.

## Introduction

In the recent years, research in the field of nanomaterials and nanotechnology have seen exponential growth due to their multiple applications in different area such as molecular imaging, drug delivery, engineering technology and development of materials and medical devices for diagnosis and treatment.<sup>1-3</sup> Various biomedical applications are owed to their attractive properties such as small size, large surface area to volume ratio, high reactivity to the living cells, flexibility in functionalization and wide range of target delivery.<sup>4</sup> Nevertheless, the

behavior of nanoparticles inside the cells is still an enigma, and not all the complexity of interactions between these particles and cells is completely understood. Therefore, the finding of appropriate experimental design and analysis methods will allow understanding the mechanisms of efficiency and toxicity of nanomaterials, so that nanomaterials could be safely used in medicine.

Usually, the changes in the chemical composition of tissues sequences are early events in pathology, their detection by modern techniques are useful in early therapeutic intervention. For this purpose, Raman spectroscopy has been shown to have the ability to distinguish between normal and pathologically altered skin samples, being a useful technique for early diagnosis. The gold standard in diagnosis of skin pathology is biopsy and histological investigations. This process is invasive and time-consuming, needs a special qualification and allows detection of lesions after their occurrence. Optical imaging systems are ideally suited for early detection of epithelial diseases, including most cancers, and for the assessment of tumor margins and therapy response. Raman spectroscopy is an optical technique based on vibrational activity of chemical bonds and has been successfully applied in pathology to differentiate a variety of lesions. This technique is able to identify the unknown substances in a tissue, based on spectral signature of mode of vibration for each molecule from a sample. In recent decades, Raman spectroscopy was used to characterize the molecular composition and hydration of normal skin and to analyse the conformational structures of proteins, water and lipids in mummified skin.<sup>5-8</sup> Several studies found the changes of protein and lipid structures in basal cell carcinoma or actinic keratosis compared to normal skin, changes which allowed to discriminate between the tissues and identify the tumour margins.<sup>9-11</sup> Moreover, based on high wave number Raman bands it is possible to separate the perilesional and normal tissue.<sup>10</sup> Such techniques are particularly relevant to inflammation, where the detection of subclinical, early disease states, could facilitate early diagnosis and targeted therapies.

It is known that inflammation is a complex biological response involved in the pathogenesis of a large variety of diseases.<sup>12</sup> Generally, in the acute inflammatory response, numerous cytokines such as tumor necrosis factor (TNF- $\alpha$ ), interleukin (IL)-1, IL-6 and pro-inflammatory enzymes (cyclooxygenase-2 [COX]-2, prostaglandin E synthase, inducible nitric oxide synthase [iNOS]) are released, inducing vasodilatation, edema, cellular metabolic stress

and even tissue necrosis.<sup>13,14</sup> Eicosanoids such as prostaglandin E2, derived from polyunsaturated fatty acids, promote angiogenesis, hinder apoptosis and stimulates the inflammation as well as the cell proliferation and growth of tumor tissue.<sup>15</sup> Consequently, the ability to detect and treat inflammation is critical for the treatment and prevention of inflammatory conditions. Moreover, the use of nanoparticles for detection of vascular activation and cellular recruitment at subclinical levels has proven effective in practice.

Gold nanoparticles (AuNPs) have been widely used as therapeutic agents in experimental gene therapy and drug delivery of anticancer agents antibiotics, amino-acids and peptides, antioxidants or isotopes.<sup>16-21</sup> Silver nanoparticles (AgNPs) are used to impregnate varied textile materials for odor reduction, in creams for acne treatment or in dressings healing.<sup>22</sup> Beside the antimicrobial action, it was shown that AgNPs exerted cytotoxic and pro-apoptotic effects mediated via reactive oxygen species (ROS), both in normal as well as in tumour cell lines.<sup>23-27</sup> Furthermore, some researchers have suggested that silver ions released from AgNPs in aqueous medium can induce inflammatory response, may interact with nucleic acids and lead to focal inflammation 14 days after topical treatment.<sup>25,28,29</sup> Although some studies have shown that AuNPs are biologically inert, there are other researches which attest that they generate inflammation, especially small nanoparticles, as a response of the host to foreign particles.<sup>30,31</sup> The inflammatory response is transient and accompanied by an increase macrophage phagocytosis and apoptosis.<sup>32</sup>

The phytochemical synthesis of metal nanoparticles with polyphenols from natural extracts could be an option to counteract the adverse reactions as they can reduce ROS production and protect the cellular proteins and lipids. The *in vivo* effects of such compounds are crucially important to be investigated before approving any potential therapeutic applications. Cornelian cherry (*Cornus mas*) could be a candidate for “green synthesis” of metal nanoparticles. It was known as medicinal plant for the treatment of inflammation in an ancient system of medicine.<sup>33</sup>

The aim of the present study was to evaluate the potential of Raman spectroscopy as a technique capable to provide the diagnosis of skin inflammatory conditions and to differentiate the effect of treatments with silver and gold nanoparticles conjugated with natural extracts compared to extract alone. Vibrational data collected from samples are presented in conjunction

with the conventional histopathological investigation, transmission electron microscopy (TEM) and assessment of prostaglandin E2 (PGE2) levels.

## Experimental

### Materials

Silver nitrate ( $\text{AgNO}_3$ ), NaOH and EDTA- $\text{Na}_2$  were obtained from Merck KGaA Darmstadt (Germany) and absolute ethanol and n-butanol from Chimopar (Bucharest). Glutaraldehyde for TEM was from EMS, (Hatfield, USA), osmium tetroxide and lambda-carrageenan type IV from Sigma-Aldrich, (St. Louis, USA) and Epon 812 resin from Fluka GmbH (Buchs Switzerland). ELISA tests for evaluation of PGE2 levels were obtained from Blue Gene (China). Standard gold solution 1000 mg/L in HCl 2 mol/L respectively standard silver solution 1000 mg/L in  $\text{HNO}_3$  0.5 mol/L were purchased from LGC Standards GmbH (Wesel, Germany).

### Vegetal material and preparation of the extract

Samples of *Cornus mas L.* (CM) fruits were collected in September 2013 from Cluj-Napoca (altitude 360 m), Romania. The species of fruits were identified by Botanical Department of the Faculty of Pharmacy Cluj-Napoca and voucher specimens were deposited in the Herbarium of the Faculty of Pharmacy, “Iuliu Hatieganu” University of Medicine and Pharmacy, Cluj-Napoca. Natural extracts were obtained according to David et al. method.<sup>34</sup> The total anthocyanins content was determined using the pH differential method and the total phenolic content was assessed by the Folin-Ciocalteu method.<sup>35,36</sup>

### Synthesis of AgNPs-CM and AuNPs-CM nanomaterials and their characterization

The AgNPs-CM and AuNPs-CM were prepared by the reduction of the metallic salts with a natural extract solution of *Cornus Mas* by the method described before.<sup>34,37</sup> The pH of natural extracts solutions is brought at 7.5 with 1M NaOH solution. The concentrations of the used solutions have been: 0.03 M  $\text{HAuCl}_4 \cdot 3\text{H}_2\text{O}$ , 0.06 M  $\text{AgNO}_3$  and natural extract with  $25 \times 10^{-3}$  mM total anthocyanins. 16.6 ml *Cornus mas* extract and 6.6 ml solution of metallic ion were

added to 200 ml double distilled water with vigorously stirring for 10 minutes, until a brown solution was obtained. The metallic nanoparticles have been kept at refrigerator until used.

The colloids were stable for 30 days after which the metallic nanoparticles aggregated very slightly. UV-Visible-NIR extinction spectra were measured in a 2 mm quartz cell using a Jasco V-670 spectrometer with 1 nm spectral resolution. The morphology and size distribution of nanoparticles were examined by a TEM JEOL-JEM 1010 instrument (JEOL Inc). The zeta potential of gold and silver nanoparticles was determined by laser Doppler micro-electrophoresis technique using a Malvern Zetasizer Nano ZS-90. The Nano ZS contains a He-Ne laser operating at a wavelength of 633 nm and an avalanche photodiode detector. The measurements were performed at a temperature of 25 °C. For biological application, besides physicochemical property characterization, the tissue toxicity and biocompatibility evaluation of nanoparticles is important. Therefore, we tested the acute systemic toxic effects of both metallic nanoparticles on Wistar rats (See Supplementary file Section S1).

### **Model of carrageenan-induced inflammation in Wistar rats**

The study was performed on an experimental model of inflammation induced by administration of carrageenan in the footpad of male Wistar rats. The animals (130-150 g) were obtained from the Animal Department of "Iuliu Hatieganu" University of Medicine and Pharmacy, Cluj-Napoca, Romania and were acclimatized under the following conditions: 12-h light/12-h dark cycles, 35 % humidity, had free access to water and were fed with a normocaloric standard diet (VRF1). Paw edema was induced by injection of a 100 µl of freshly prepared 1 % carrageenan ( $\lambda$ -carrageenan, type IV, Sigma) diluted in normal saline in the right hind footpad.<sup>37</sup> The left hind foodpad was injected with the same volume of saline solution. One dose of nanoparticles suspension functionalised with the *Cornus Mas* extract was administered orally 1 day prior to injection of carrageenan, in a volume not exceeding 0.25 ml. We used 5 groups each consisting of 8 animals divided as follows: group 1 – normal, control tissue; group 2 – animals with inflammation pre-treated with 0.9 % NaCl solution as a positive control group; group 3 – inflammation pre-treated with AuNPs-CM 0.3 mg/b.w.; group 4 – inflammation pre-treated with AgNPs-CM 0.3 mg/b.w.; group 5 – inflammation pre-treated with 15 mg/b.w./day *Cornus Mas* extract. At 24 hours after carrageenan administration, soft paw tissues were sampled and used for

Raman spectroscopy and histopathological investigations. For quantification of metal content in sample, transmission electron microscopy and evaluation of prostaglandin E2 levels by ELISA, the paw tissues were sampled after 4 and 24 hours.

### **Samples preparation**

For Raman analysis fresh biopsies from the paws of sacrificed mice were immediately immersed in Jung Tissue Freezing Medium (Leica Biosystems). They were cryo-sectioned maximum within 2 hours after sampling at a thickness of 10 $\mu$ m, using a Leica CM 1850 Cryotome set at -20 °C. One section from each animal from each group was placed on normal histology glass slides then placed in an incubator for drying and better adherence at (37 °C for 1 hour). Samples were then stored in a freezer at - 20 °C until tissue analysis using confocal Raman imaging. Following Raman spectroscopy analysis of the paw, the same sections were photographed unstained, then stained H&E and photographed again using a BX51 microscope, DP 25 digital camera and the Olympus Cell B software. Each microscopical section evaluated had a surface of 330.68  $\times$  421.42  $\mu$ m. For ELISA investigations the soft tissue homogenates were prepared in 50 mM TRIS–10 mM EDTA buffer (pH 7.4) and homogenized with a Polytron homogenizer (Brinkman Kinematica, Switzerland) as previously described.<sup>34</sup>

### **Determination of Au and Ag levels by atomic absorption spectrometry**

The analysis of gold and silver nanoparticles content in paw tissues were conducted by atomic absorption spectrometry using an AVANTA PM atomic absorption spectrometer (GBC Scientific Equipment, Braeside, Australia) equipped with a graphite furnace (GF 3000) and programmable auto-sampler (PAL 3000, GBC Scientific Equipment, Braeside, Australia). Additionally, pyrolytic graphite furnaces (P 301, Photron Ltd. Victoria, Australia), gold cathode lamp (P 821 HCl) respectively silver and deuterium lamps were used. Calibration was performed using the "Linear Least Squares" method and was obtained an excellent correlation for 0-50  $\mu$ g/L gold (R = 0.9997) and 1-6  $\mu$ g /L silver (R = 0.9996). Prior to the determination, the biological samples were mineralized in 1 mL *aqua regia* for gold and nitric acid for silver, at room temperature. Each sample was measured three times. The corresponding calculated concentrations in metal nanoparticles were: 1.96  $\mu$ g/g tissue for AuNPs-CM at 4 hours, 2.95

$\mu\text{g/g}$  tissue at 24 hours, 1.62  $\mu\text{g/g}$  tissue for AgNPs-CM at 4 hours and 1.96  $\mu\text{g/g}$  tissue at 24 hours.

### **Raman spectroscopy**

The Raman spectra and images presented in this work were recorded using a Confocal Raman Microscope (alpha 300 R from WITec GmbH, Ulm, Germany) equipped with a Nd-YAG laser working at 532 nm and an ultrahigh throughput spectrometer (UHTS 300) for Raman light analysis. A 100x dry microscope objective with a numerical aperture (NA) of 0.9 was used to perform all measurements from tissues. The Raman backscattered light collected through the objective was passed through a holographic edge filter, before being focused into a multimode optical fiber of 100  $\mu\text{m}$  diameter which provides the optical pinhole for confocal measurement. The light emerging from the output optical fiber was analyzed by an ultrahigh throughput spectrometer equipped with back-illuminated deep-depletion 1024  $\times$  128 pixel CCD camera (DV<sub>401</sub>-BV, Andor) operating at  $-60$  °C. The tissues placed on glass slides were mounted on a piezoelectric scanning stage and scanned through the laser focus in a raster pattern. The spectroscopic imaging was performed over a 150  $\times$  150  $\mu\text{m}^2$  area which was first divided into four squares of 75  $\times$  75  $\mu\text{m}^2$  (75  $\times$  75 pixels) selected from the unstained glass slide sections. Each square was imaged with an integration time of 0.5 s for each spectrum to prevent sample degradation at the focal point. The measurements were conducted at a power incident on the samples of 10 mW. The WITec Project Plus software was used for spectral analysis and image processing. Reflected-light bright-field optical images of tissues were captured with a color video camera attached to the eyepiece out-port of the same microscope using for illumination a super-bright white LED source.

### **Transmission electron microscopy**

For transmission electron microscopy the paw tissues were fixed for 1.5 hour with 2.7 % glutaraldehyde, washed four times with 0.1 M phosphate buffer (pH 7.4), post fixed for 1.5 hour with 1.5 % osmium tetroxide, dehydrated in an acetone series, and embedded in Epon 812 resin as previously described.<sup>34</sup> The ultrathin sections obtained with glass knives using a Bromma 8800 ULTRATOME III (LKB, Stockholm, Sweden) were collected on 300 mesh copper grids

(Agar Scientific Ltd., Stansted, UK). The samples were examined on a JEOL JEM 1010 transmission electron microscope (JEOL Ltd., Tokyo, Japan) at 80 kV acceleration voltage, and photographed with a Mega VIEW III camera (Olympus, Soft Imaging System, Münster, Germany).

### **Prostaglandin (PG) E2 levels**

PGE2 contents of tissue homogenates were measured using ELISA system (Blue Gene, China) according to the manufacturer's instructions. Results are expressed as pg/mg protein.

### **Statistical analysis**

Experimental data were analyzed by one-way analysis of variance (ANOVA) followed by the Tukey's multiple comparisons post test using GraphPad Prism 5.0 software (GraphPad, San Diego, Ca., SUA). All values are expressed as mean  $\pm$  standard deviation, with a limit of statistical significance of  $p < 0.05$ .

## **Results and discussion**

### **Characterization of nanomaterials**

Detailed characterization of the nanoparticles morphology was obtained by TEM measurements. Fig. 1A, B illustrates representative TEM pictures of obtained nanoparticles, which clearly reveals that the products as prepared are mainly composed of spherical nanoparticles dispersed in solution with the particle diameter of 13 - 52 nm for AuNPs-CM and 20 - 100 nm for AgNPs-CM, respectively.

The optical absorption spectra of as prepared nanoparticles in Fig. 1C exhibit a dominant plasmonic band centered at 409 nm for AgNPs-CM (curve a) and at 525 nm for AuNPs-CM (curve b), which represents the typical signature of the dipolar plasmon resonance of individual spherical silver and gold nanoparticles, respectively.<sup>39</sup>

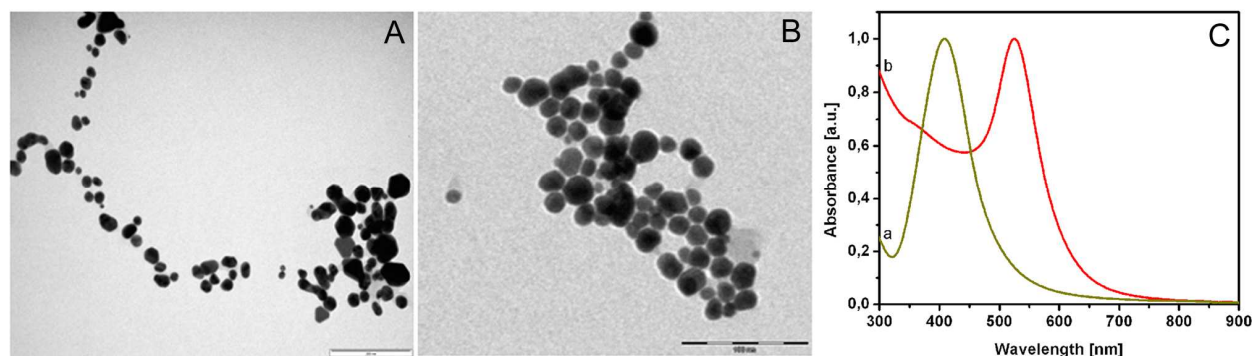


**Fig. 1** Transmission Electron Micrographs of: (A) NPs-CM and (B) AgNPs-CM. (C) Normalized absorption spectra of: (a) AgNPs-CM and (b) AuNPs-CM

The performance of colloidal nanoparticles in different applications strongly depends on their chemical stability. The stability of colloidal systems is defined in terms of the charge on their surface. The zeta potential distribution of the prepared nanoparticles is relatively narrow and centered at - 19.7 and - 22.4 mV for AuNps-CM and AgNps-CM, respectively indicating a good stability of nanoparticles in colloidal suspension (result not shown). In view of next step toward applications we further investigated the sample stability in simulated physiological conditions by mixing 500 mL of colloidal solution with 100 mL of a solution of PBS/PBS containing 10% fetal bovine serum. We found that the absorption spectra of mixed samples remained stable after 4 h of incubation (more details in the Supplementary file, Section S2). The acute systemic toxicity test performed on Wistar rats revealed a transient toxicity in liver, induced especially by high doses of AgNPs-CM nanoparticles (See Supplementary file, Section S3 and S4).

### Confocal Raman microscopy

As stated above, confocal Raman microscopy is a powerful spectral imaging tool for investigation of molecular composition in a non-destructive and label-free manner. We used Raman spectral micro-imaging combined with multivariate statistical analysis to detect and visualize subtle biochemical changes in tissues associated with pathologically altered skin and to evaluate the effect of different therapeutic agents.

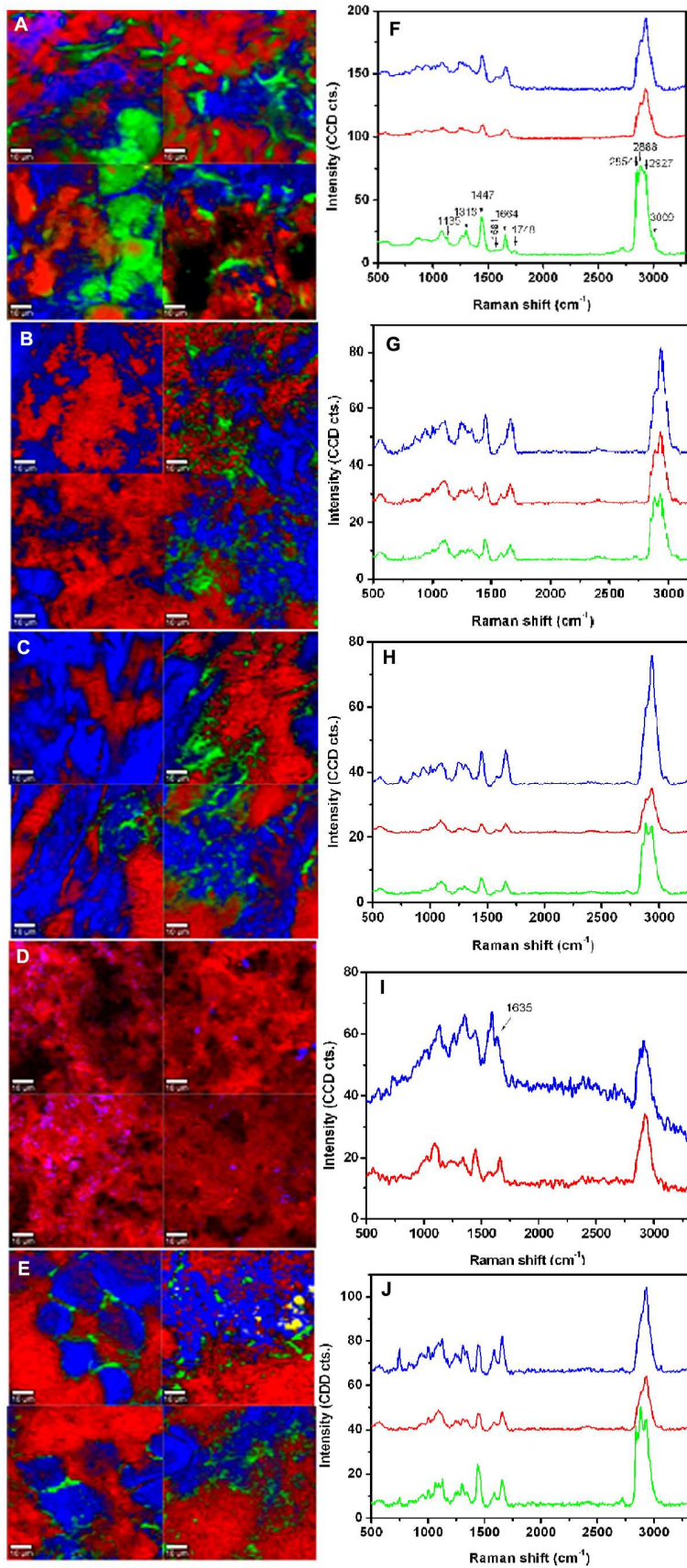


**Fig. 2** Raman maps obtained by multivariate data analysis algorithms (K-means cluster analysis) of: (A) normal skin tissue; (B) inflamed skin tissue and treated tissues with AuNPs-CM (C) and AgNPs-CM (D) and CM extract (E). The scale bar is 10  $\mu\text{m}$ . Corresponding extracted spectra from distinctly colored areas in images: (F) normal skin tissue; (G) inflamed skin tissue and treated tissues with AuNPs-CM (H), AgNPs-CM (I) and CM (J)

The acquired two-dimensional Raman spectral maps were processed with K-means cluster algorithm that allows the classification of the skin tissue histological organization based on the intrinsic biochemical composition. K-means cluster analysis enables the partition of the spectra within a Raman image into a predefined number of groups of similar biochemical characteristics and to construct color-coded spectral images. A mean spectrum of each cluster within an image dataset was derived and overlaid for spectral comparison. This method was previously described ref. 40.

Fig. 2 shows representative multivariate Raman spectral images of normal soft paw tissue (A), inflamed tissue treated with vehicle (B) and tissues treated with AuNPs-CM (C), AgNPs-CM (D) and CM (E). The presented Raman images facilitate the identification of the main histological features of the soft paw tissue and enable the visual discrimination between healthy, inflamed and treated tissues. Indeed, the distribution of proteins (red cluster), lipids (blue cluster) and unsaturated fatty acids, lipids-reach (green cluster) regions highlights obvious visual differences between the analyzed skin tissues. To identify the origin of the visual differences and hence the biochemical alterations we compared the corresponding extracted spectra of tissue samples presented in Fig. 2F-J. The Raman spectrum of the normal paw tissue in Fig. 2F shows vibrational bands at 862, 926, 1093, 1125, 1248, 1316, 1447, 1581, 1664, 1748, 2854, 2888, 2927 and 3009  $\text{cm}^{-1}$ . The assignment of Raman fingerprint of the tissue is given in Table 1 which is in good agreement with other similar data published in the literature.<sup>41,42</sup>

The biochemical differences between the analyzed samples appeared to show a strong association with the spectral region of 2800-3100  $\text{cm}^{-1}$  originating from the vibrations of the lipids, unsaturated fatty acids and proteins (green cluster). Previous studies have demonstrated that the vibrations characteristics from unsaturated fatty acids play a leading role in

distinguishing between cancerous and noncancerous human tissues.<sup>41,43</sup> In accordance to these findings, in the first step we carefully analyze the distribution of oleic acid, linoleic acid,  $\gamma$ -linoleic acid and arachidonic acid. The Raman profile of the normal soft paw tissue in the region of 2800-3100  $\text{cm}^{-1}$  is dominated by the vibrational bands at 2854, 2888, 2926 and 3009  $\text{cm}^{-1}$  (Fig. 2F, green curve). The position and the ratio between the intensities of these bands are very similar to the Raman signature of oleic acid and linoleic acid, according to the literature.<sup>41,43</sup> In contrast, the Raman profile of the inflamed tissue in the region of 2800-3100  $\text{cm}^{-1}$  (Fig. 2G, green curve) shows noticeable differences related to the vibrational bands at 2854 and 2926  $\text{cm}^{-1}$ . Specifically, a significant decrease of the intensity of the peak at 2854  $\text{cm}^{-1}$  with a concomitant increase of the intensity of the peak at 2926  $\text{cm}^{-1}$  is clearly visible in the case of inflamed tissue. The comparison with the Raman spectra of the unsaturated fatty acids shows that the inflamed paw soft tissue is dominated by the Raman signature of  $\gamma$ -linoleic acid and arachidonic acid.<sup>41,43</sup> In addition, the corresponding multivariate Raman images shows that the normal tissue contains a markedly higher concentration of unsaturated fatty acids as compared to that of inflamed skin and subcutaneous tissue (Fig. 2A, B, green cluster).

Raman ( $\text{cm}^{-1}$ )	Tentative assignment <sup>40,41</sup>
862	proline, collagen (CC stretching)
926	ribose-phosphate (CO and CC stretching)
1093	phospholipids (symmetric stretching $\text{PO}_2$ , stretching CC, stretching COC) glycosidic link
1125	glycogen (CO stretching from $\text{CH}_2\text{OH}$ of carbohydrates); carotenoids (CC stretching)
1248	amide III, $\alpha$ -helix, collagen, tryptophan (stretching CN, bending NH); phospholipids (asymmetric stretching $\text{PO}_2$ ); nucleic acids (ring stretching)
1316	$\beta$ -D-glucose, D-(+), dextrose ( $\text{CH}_2$ and $\text{CH}_2\text{OH}$ deformations); amide III, $\alpha$ -helix (NH and CH bands)
1447	lipids ( $\text{CH}_2$ scissoring, $\text{CH}_2$ deformation); phospholipids ( $\delta$ ( $\text{CH}_2$ ) scissoring); collagen ( $\delta$ ( $\text{CH}_2$ ), $\square$ $\delta$ ( $\text{CH}_3$ ))
1581	tryptophan, proteins (NH bending amide II, C-N stretching)
1664	amide I/ $\alpha$ -helix (H-bonded CO stretching); unsaturated bonds of lipids (C=C stretching)
1748	lipids (C=O stretching)
2854	fatty acids, lipids (CH stretching, $\text{CH}_2$ symmetric stretching)
2888	fatty acids, lipids (CH, $\text{CH}_2$ asymmetric stretching)
2926	fatty acids, lipids, polypeptide ( $\text{CH}_2$ asymmetric stretching); proteins (CH stretching, $\text{CH}_3$ symmetric stretching)
3009	fatty acids, lipids (H-C=C stretching)

**Table 1.** Assignments of the major Raman bands of the normal skin tissue

It is known that oleic acid is a common monounsaturated acid found in various animal and vegetable fats while the polyunsaturated fatty acids are precursors of eicosanoids released from phospholipid cell membranes as a result of phospholipase A<sub>2</sub> action. Eicosanoids including prostaglandin (PG), prostacyclin (PGI) and thromboxanes (TX), synthesized under the cyclooxygenase (COX) activity and leukotrienes (LT), are involved in inflammation and allergic reactions as well as in cell proliferation and growth of tumor tissue.<sup>44-46</sup> Arachidonic acid is a key inflammatory intermediate which is released immediately after induction of inflammation, before the recruitment of leukocytes and the infiltration of immune cells at inflammatory site. It is very susceptible to lipid peroxidation and generates cytotoxic compounds subsequent their action on the macromolecules of cells such as proteins, nucleic acids and lipids. The compounds which are formed in turn amplify the inflammation.<sup>46</sup>

Colloidal gold and silver nanoparticles can selectively accumulate into pathologically altered tissues by a phenomenon termed the enhanced permeability and retention (or EPR) effect and represent an alternative for developing reliable delivery systems for targeting drugs at a specific site in a desired concentration.<sup>47</sup> As observed in Fig. 2C (green cluster), the oral administration of AuNPs-CM leads to an increase in the concentration of unsaturated fatty acids. The effect of AuNPs-CM is associated with marked biochemical changes in the spectral region of 2800-3100 cm<sup>-1</sup>. Specifically, a decrease of the intensity of the band at 2926 cm<sup>-1</sup> with a concomitant slight increase of the intensity of the band at 2854 cm<sup>-1</sup> is clearly shown after the oral administration of the AuNPs-CM (Fig. 2H, green curve). The comparison with the Raman signature of normal and inflamed skin tissue shows that the spectral profile of the treated skin tissue tends to reproduce the Raman spectrum of the normal skin tissue. In contrast, after the oral administration of AgNPs-CM, there is no amount of detectable unsaturated fatty acids (Fig. 2D – the lack of green cluster). The corresponding Raman profile in the region of 2800-3100 cm<sup>-1</sup> (Fig. 2I) confirms that the vibrations originating from unsaturated fatty acids are no longer discernible after the treatment with AgNPs-CM. It appears that this result could be surprising in the lack of Raman signal from unsaturated fatty acids. However, this can be explained by the fact that the Raman bands in the spectral region of 2800-3100 cm<sup>-1</sup> originate not only from the vibrations of unsaturated fatty acids, but also from lipids and proteins. It is therefore conceivable that the inflamed skin tissue treated with AgNPs-CM contains a lower concentration of

unsaturated fatty acids and a markedly higher concentration of proteins or lipids as compared to that of inflamed tissue. This, in turn masks the spectral signature of unsaturated fatty acids. Indeed, the multivariate Raman images of the inflamed skin tissue treated with AgNPs-CM in Fig. 2D clearly shows a noticeable contribution from proteins (red cluster). It was previously reported that the distribution of proteins plays a crucial role in distinguishing between normal and pathologically altered skin. As it can be seen in Fig. 2A (red cluster) the normal skin tissue contains a much lower concentration of proteins in comparison with the tissue treated with AgNPs-CM. This finding was previously explained by increased synthesis of large amounts of proteins in inflammatory and proliferating tissues.<sup>41,43</sup> A detailed inspection of the red cluster in Fig. 2A-E shows that this overgrowth of protein concentration occurs only in the inflamed skin tissue treated with AgNPs-CM. Moreover, the normal skin tissue in Fig. 2A is characterized by well-differentiated regions associated to the distribution of proteins (red cluster), lipids (blue cluster) and unsaturated fatty acids (green cluster). In contrast, the inflamed skin tissue treated with AgNPs-CM is devoid of this organization and is characterized by only two spectral zones. The blue cluster in Fig. 2D is associated with the occurrence of the vibrational band at  $1635\text{ cm}^{-1}$ . This spectral feature was previously assigned to a conformational change in the protein secondary structure.<sup>48</sup> Interestingly, the zones corresponding to the protein denaturation are highly localized and are observed only in the inflamed skin tissue treated with AgNPs-CM (Fig. 2D, blue cluster). Overall the above results indicate that AgNPs-CM induce inflammatory and cytotoxic effects on the skin tissue after oral administration, while AuNPs-CM exhibit moderate anti-inflammatory properties. As observed in Fig. 2E (green cluster), the treatment with CM extract leads to a slight increase in the concentration of unsaturated fatty acids. The biochemical changes in the spectral region of  $2800\text{-}3100\text{ cm}^{-1}$  are very similar to those induced by AuNPs-CM (Fig. 2H, J, green curve). We can assume that the anti-inflammatory effect of the CM extract is lower as compared to the effect of AuNPs-CM. CM was reported to possess antioxidant and anti-inflammatory effects and diminished the structural changes in tissues induced by inflammation.<sup>49,50</sup> By analyzing the spectral region of  $2800\text{-}3100\text{ cm}^{-1}$  our results suggest that CM exhibits only a low anti-inflammatory effect after the oral administration. A possible explanation for the limited efficiency is the low concentration of the CM extract at the site of inflammation.

### **Histopathological analysis and transmission electron microscopy**

Oral delivery is the most common method for drug administration. It is known that, under normal healthy conditions, nanoparticles administered orally cross very difficult the mucus barrier of gastrointestinal tract, capillary endothelium and extracellular matrix (ECM) to reach the target cells. However, in inflammation, endothelial cells lose the cellular integrity due to the activation of proinflammatory cytokines, increase angiogenesis and over-expression of cell receptors, factors which facilitate the accumulation of nanoparticles at target site, so-called the enhanced permeability and retention (EPR) effect.<sup>51-54</sup> This ability in conjunction with antioxidant and anti-inflammatory effects of natural compounds used for functionalization are exploited in the present work.

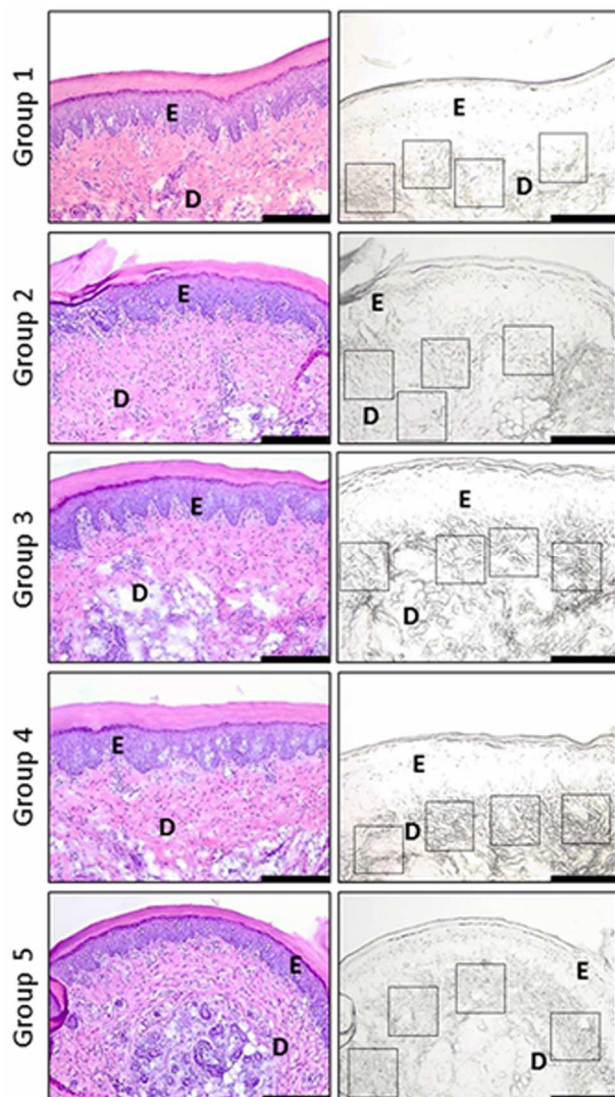


**Fig. 3** Parallel evaluation of H&E-stained (left column) and unstained (right column) paw biopsies from the 5 groups. Each section has a surface of  $330.68 \times 421.42 \mu\text{m}$ . Different degrees of perivascular and interstitial edema as well as varying intensities of inflammatory cells in the dermis, mainly macrophages with a few neutrophils, was observed. These changes were more intense in Groups 2 and 4, less intense in Groups 3 and 5. Normal histological aspect was observed in group 1. The dotted squares represent the 4 areas of  $75 \times 75 \mu\text{m}$  used for Raman analysis. (E = epidermis; D = dermis). Scale bar is  $100 \mu\text{m}$ .

To assess the ultrastructural paw tissue changes after oral metal nanoparticles in acute inflammation, conventional histology and TEM were used. In Fig. 3 the left panel is showing the hematoxylin-eosin stained sections of paw tissues. In group 1 we observed a section of normal paw tissue containing a keratinized squamous epithelium covered by a homogenous thick orthokeratin layer, rete ridges, dermal papilla, loose irregular connective tissue (papillary dermis) and dense irregular connective tissue with closely packed collagen fibers (reticular dermis). Some blood vessels are also visible in the dermis. On this background, in groups 3 and 5 a minimum amount of inflammatory cells (macrophages and a few neutrophils) was observed in the dermis accompanied by minimal edema, mainly perivascular. In group 4 (AgNPs-CM) perivascular edema was more prominent and more inflammatory cells were observed infiltrating the dermis. Similar changes but more severe (increased cellularity in the dermis as well as perivascular and interstitial edema) were observed in rats from group 2 (vehicle treatment). Histological, on H&E stain, edema is observed as clear spaces, occupied by interstitial fluid, whereas macrophages are seen as round to oval cells with basophilic nuclei. For all images, the unstained tissue section (Fig. 3, right column) showed similar architecture, with the collagen fibers being more prominent (dark fibrillar appearance) and the squamous epithelial cells being paler.

Ultrastructure of papillary region of dermis was investigated in all the experimental groups by transmission electron microscopy (TEM), with regard to its interface with the basal membrane and with the keratinocytes from stratum basale of epidermis, the aspect of blood capillaries, number and distribution of fibroblasts and other cells, and aspect and density of collagen network. In the untreated, control group (group 1), the normal ultrastructure of dermis was observed. The superficial region of the papillary dermis was immediately subjacent and tightly attached to a thin and continuous basement membrane underlying the cells from stratum basale. This region contained relatively dense packed collagen bundles, crossing in all directions and a few extensions of fibroblasts (Fig. 4A).

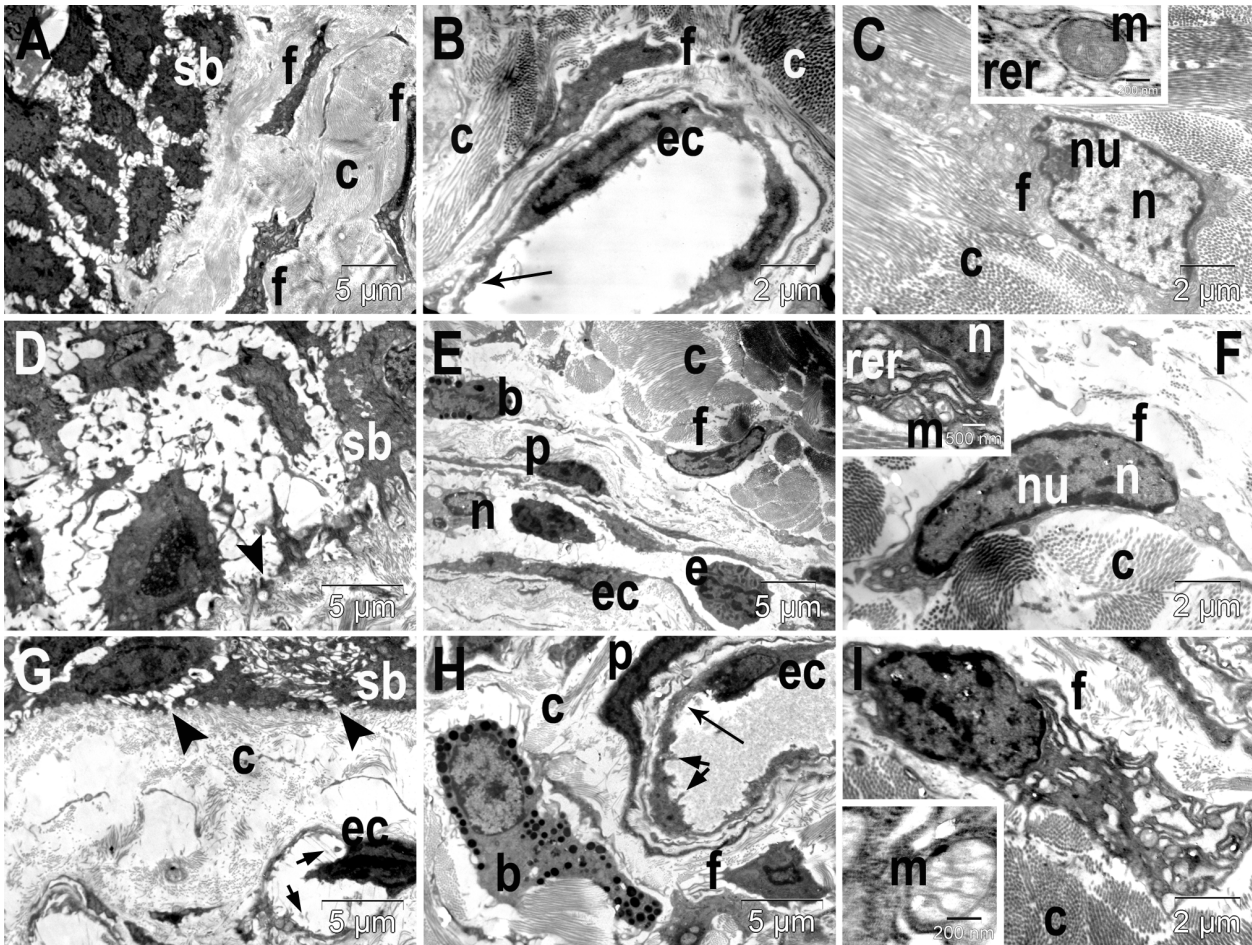


**Fig. 4** TEM images of rat papillary dermis from negative controls (group 1, A-C), positive controls – carrageenan induced inflammation after 4 h (group 2, D-F), and positive controls after 24 h respectively (group 2, G-I). A: normal ultrastructure of epidermis-dermis interface; D, G: the abnormal ultrastructure of epidermis-dermis interface; B: capillaries with normal aspect of epithelium; E, H: modified aspect of capillaries; C: normal ultrastructure of fibroblasts; F, I: fibroblasts with changed ultrastructure and function. sb-stratum basale; c-collagen bundles; f-fibroblasts; ec-endothelial cells; m-mitochondria; rer-rough endoplasmic reticulum; p-pericytes; arrowheads-regions of interruption in the basement membranes; long arrows-pinocytosis vesicles; short arrows-extensions of epithelial cells into the lumen.

Capillaries were surrounded by pericytes (not shown) and endothelial cells had elongated, euchromatic nuclei with regular outline. They also presented flat prolongations and a relative low number of transecytosis vesicles dispersed into their cytoplasm (Fig. 4B). Capillaries were closely surrounded by the collagen fibers network, and rare extensions of fibroblasts. The fibroblasts showed big, euchromatic nuclei, with more or less irregular contour, and prominent nucleoli. In their cytoplasm, many profiles of rough endoplasmic reticulum were present, as well as several round, or oval mitochondria, and sometimes Golgi apparatus was observed (Fig. 4C). The collagen fibers were in tight contact with the fibroblasts.

In the group with inflammation pre-treated with vehicle important ultrastructural changes were identified at 4 hours. The basal layer of epidermis was disorganized, as well as several layers of keratinocytes in stratum spinosum. The basement membrane appeared discontinued in some images, and the density of collagen fibers adjacent to it was reduced (Fig. 4D). Capillaries had a thinner endothelium, and sometimes the endothelial cells were prominent into the lumen (not shown). Many granulocytes were observed within the capillaries, and also in their immediate vicinity (Fig. 4E). The collagen network around the capillaries had a general reduced density, even though some denser packed bundles were identified. The fibroblasts still showed euchromatic nuclei and prominent nucleoli, but the perinuclear space was distended. Vacuolated rough endoplasmic reticulum and swollen mitochondria were observed in their cytoplasm (Fig. 4F). The fibroblasts were surrounded by large electron-lucent halos due to the absence of collagen fibers, mainly in regions close to epidermis. In the same group, the ultrastructural changes were still important at 24 hours, but without the same amplitude as at 4h hours. Thus, a very low density of collagen fibers was observed, both at the interface with epidermis (Fig. 4G), and deeper in the dermis (Fig. 4H, I).

The most representative ultrastructural feature of the fibroblasts in this group was the large volume of rough endoplasmic reticulum that sometimes appeared as electron-transparent vesicles of various shapes and sizes (Fig. 4I). Swollen mitochondria were also observed. The collagen fibers were denser and consequently the halos around the fibroblasts were smaller. The large halos around the fibroblasts could be explained either by an interruption of collagen synthesis due to the toxic effect of the inflammatory mediators, or to a migration of fibroblasts in areas devoid of collagen in order to repair the lesions.

It was reported that carrageenan injection causes paw edema in rats in two phases, an initial phase up to 6 hours and a late phase extending up to 24 hours. The early phase is characterized by release of histamine and serotonin, both responsible for vasodilatation and increased permeability of capillaries, and the late phase is due to the action of bradykinin, prostaglandins, neutrophil-derived ROS, nitric oxide, cytokines, proteases and lysosomal enzymes, compounds which amplify the acute tissue inflammation.<sup>55-57</sup> Besides these, in the rat, a soft tissues edema fluid accumulates and neutrophil extravasations appears, changes which amplify the halos around the fibroblasts and induce swelling of mitochondria and endothelial cells.<sup>58,59</sup>

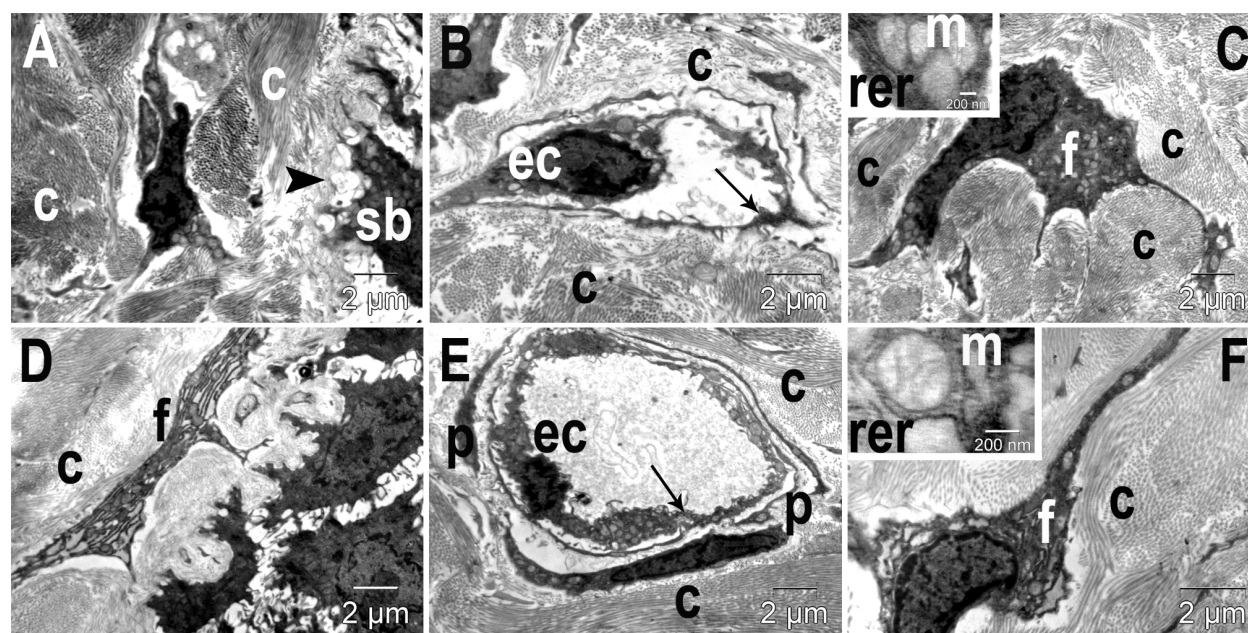


**Fig. 5** TEM images of rat papillary dermis showing low amplitude of ultrastructural changes after carrageenan induced inflammation and treatment with AuNPs-CM for 4 h (group 3, A-C), and even lower after the 24 h treatment (group 3, D-F). A, D: epidermis-dermis interface; B, E: ultrastructure of capillaries; C, F: ultrastructure of fibroblasts. sb-stratum basale; c-collagen bundles; f-fibroblasts; ec-endothelial cells; n-nucleus; nu-nucleolus; m-mitochondria; rer-rough endoplasmic reticulum; b-basophils; e-eosinophils; n-neutrophils; p-pericytes; arrowhead-interruption in the basement membranes; long arrows-pinocytosis vesicles.

In the experimentally treated groups, the ultrastructural aspect of dermis ranged between that of control group and of the positive group, treated with vehicle. In group 3 (with inflammation which received AuNPs-CM) ultrastructural changes of low amplitude were identified at 4h after induction of inflammation. Thus, at the dermoepidermal interface, rare and localized lesions in the basement membrane were noted, associated with a certain degree of disorganization of basal layer, and of collagen layer underlying the basement membrane (Fig. 5A). Capillaries displayed endothelial cells with fine extensions into the lumen and low number of transcytosis vesicles (Fig. 5B). Granulocytes were not observed, either inside or outside the capillaries. The collagen bundles had a reduced density around the capillaries (Fig. 5A) and leaved small halos around the fibroblasts (Fig. 5A-C). The fibroblasts showed normal ultrastructure, excepting the mitochondria, which were swollen, and with rarefied matrix (Fig. 5C). After 24 hours we noticed the lowest level of ultrastructural changes among the all treated groups. In most of the regions of dermis, the collagen bundles were more densely packed (Fig. 5D-F), even though some of the fibroblasts were partially surrounded by thin clear zones, devoid of collagen (Fig. 5D,F). As compared to the same group at 4 hours, the fibroblasts contained a significant higher amount of rough endoplasmic reticulum, also with larger volume. Some mitochondria were swollen and contained rarefied matrix (Fig. 5F).

In group 4, with inflammation treated with AgNPs-CM, lesions are produced at 4 hours after carrageenan injection, both in the most superficial layer of collagen (Fig. 6A), and in the capillaries (Fig. 6B). Granulocytes were observed in the proximity of capillaries (Fig. 6B) as well as at different distances from the blood vessels (not shown). Fibroblasts had low amounts of rough endoplasmic reticulum, swollen mitochondria and many vacuoles (Fig. 6C). Collagen fibers were dispersed, having reduced density around the capillaries (Fig. 6B). They were also present in low amount next to the fibroblasts (Fig. 6A-C), but without forming well delimited halos. These structural changes could be explained by cellular uptake of nanoparticles and ability to induce oxidative reaction by release of silver ions and dysfunction of mitochondria, with generation of free radicals.<sup>60</sup> They are extremely reactive; attack biological molecules situated within diffusion range and modulate intracellular calcium concentrations, activate transcription factors and induce cytokine production which in turn lead to production of reactive oxygen and nitrogen species and initiation of inflammation.<sup>61,62</sup>

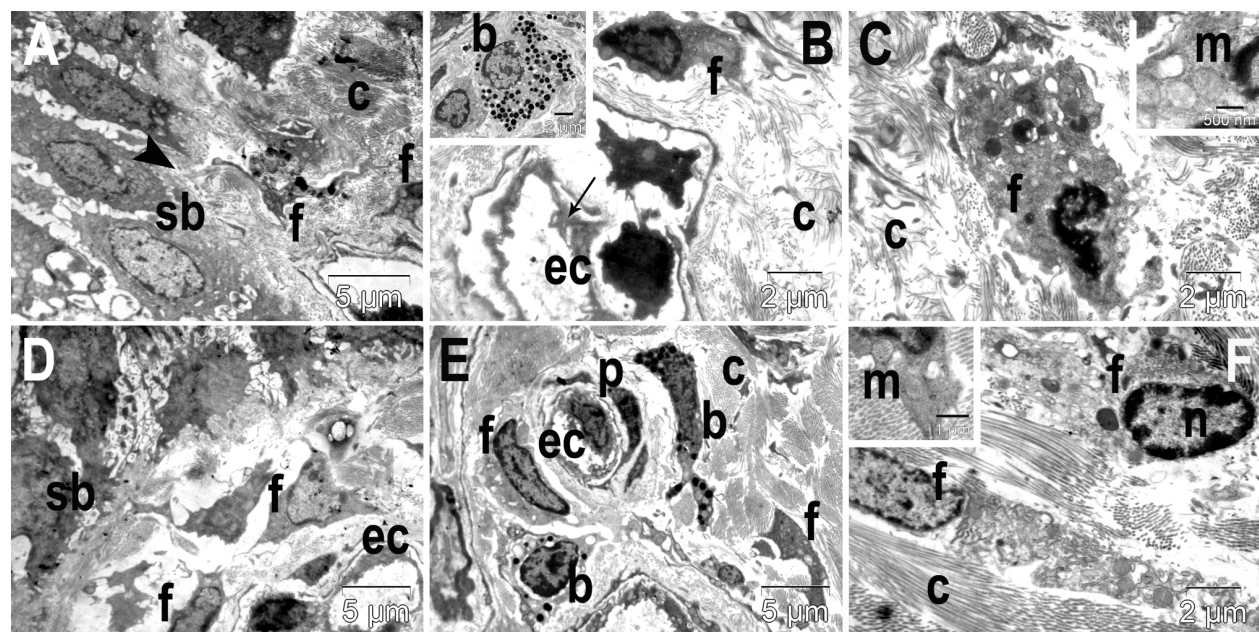


**Fig. 6** TEM images of rat papillary dermis presenting important ultrastructural changes after carrageenan induced inflammation and treatment with AgNPs-CM for 4 h (group 4, A-C), and more accentuated after the 24 h treatment (group 4, D-F). A, D: epidermis-dermis interface; B, E: ultrastructure of capillaries; C, F: ultrastructure of fibroblasts. sb-stratum basale; c-collagen bundles; f-fibroblasts; ec-endothelial cells; n-nucleus; m-mitochondria; b-basophils; p-pericytes; arrowhead-interruption in the basement membranes; long arrow-pinocytosis vesicles.

Highlighting the direct accumulation of particles is difficult, firstly due to their extremely low concentration in tissue after oral administration. The results obtained at ICP-MS confirmed these features. Furthermore, the discrimination between metal nanoparticles and structural components of paw tissue was extremely difficult in a grey-scale background. Probably would be necessary to examine the nanoparticles in tissues by using a microscope operating at higher voltage and higher magnification or by analytical microscopic methods such as energy filtered TEM (EFTEM).<sup>63,64</sup>

At 24 hours, the lesions were more accentuated, with presence of low amounts of collagen under the basement lamina of stratum basale, area very rich in fibroblasts (Fig. 6D). Granulocytes were present outside the capillaries, surrounded by discontinuous collagen bundles

(Fig. 6E). Fibroblasts observed as intact were strongly affected, while others undergone extensive damage, with plasma membrane breakdown, dilatation of perinuclear space and vacuolation of cytoplasm (Fig. 6F). Swollen mitochondria, with rarefied matrix also contributed to this appearance. Superoxide anion produced in mitochondria was reported to trigger inflammasome formation in specific specialized subdomain of the endoplasmic reticulum (ER) membrane that regulates ER-mitochondria communications called mitochondria associated ER membrane (MAMs).<sup>65,66</sup> TEM analysis revealed mitochondrial swelling and membrane damage after AgNPs-CM administration, and also granulocyte extravasations, markers of inflammation.

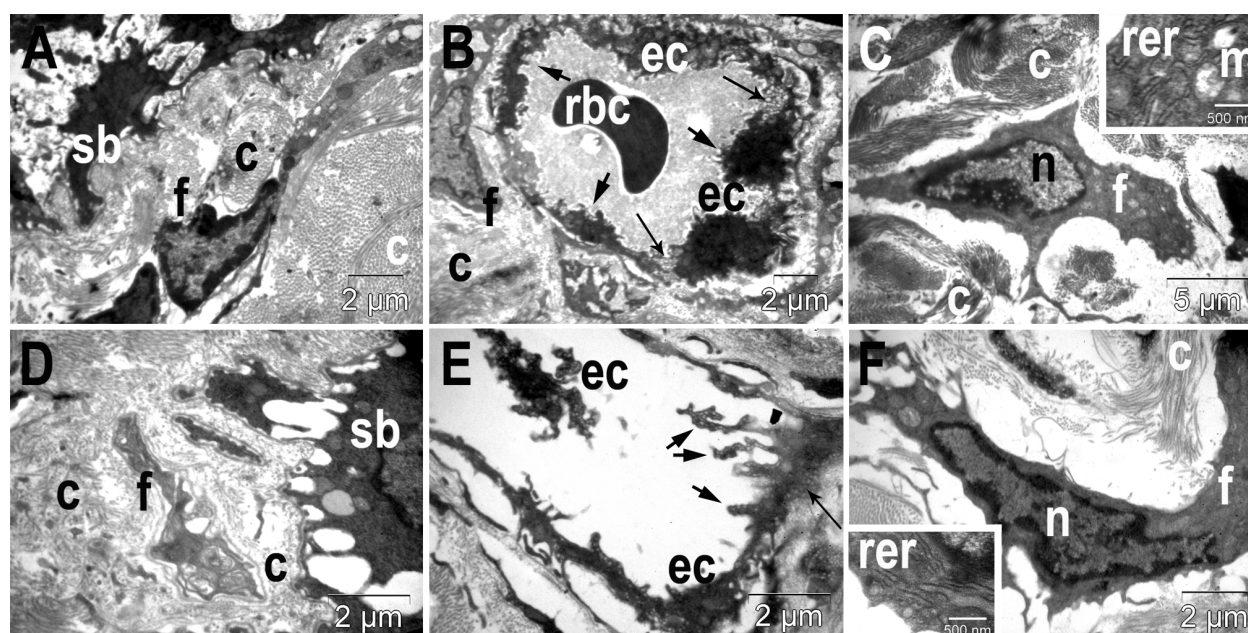


**Fig. 7** TEM images of rat papillary dermis presenting some ultrastructural changes after carrageenan induced inflammation and treatment with CM extract for 4 h (group 5, A-C), and extensive ultrastructural lesions after the 24 h treatment (group 5, D-F). A, D: epidermis-dermis interface; B, E: ultrastructure of capillaries; C, F: ultrastructure of fibroblasts. sb-stratum basale; c-collagen bundles; f-fibroblasts; ec-endothelial cells; rbc-red blood cell; n-nucleus; m-mitochondria; rer-rough endoplasmic reticulum; long arrows-pinocytosis vesicles; short arrows-extensions of epithelial cells into the lumen.

In the group 5, with inflammation treated with CM extract, after 4 hours, the general ultrastructure of the dermis showed similarities with that observed in the group treated with AuNPs-CM. Basement membrane at the interface between dermis and epidermis had small interruption zones, and the superficial collagen bundles had a relative high density (Fig. 7A). Capillaries presented a continuous endothelium with an intense traffic of endocytosis vesicles, but also with fine extensions towards the lumen. They were surrounded by dense bundles of collagen (Fig. 7B). Fibroblasts preserved in general an almost unaffected ultrastructure, excepting rare swollen mitochondria (Fig. 7C). Many of the fibroblasts also had halos of various sizes around them. After 24 hours, in the same group, the dermis resembled more with that of animals treated with vehicle at 24 hours, presenting relative extensive ultrastructural lesions. However, the density of the collagen bundles was increased next to the epidermis interface (Fig. 7D) and around the capillaries (Fig. 7E). The endothelial cells, containing many transcytosis vesicles, extended long prolongations into the lumen, and often endothelial cells or fragments of endothelial cells were found in the capillary lumen (Fig. 7E). Fibroblasts appeared with normal ultrastructure, but many were surrounded by large clear halos (Fig. 7F).

### **Quantitative estimation of PGE2 levels by ELISA**

In order to evaluate the biological impact of gold and silver nanoparticles administration on arachidonic acid metabolites generation we quantified the PGE2 levels in the paw tissue homogenate. Induction of inflammation with carrageenan increased PGE2 levels in paw tissue, both at 4 and 24 hours, compared to control group, but statistically insignificant ( $p > 0.05$ ) (Fig.8). Preadministration of AgNPs-CM induced secretion of PGE2 in soft tissue, early after injection of carrageenan, compared to control, untreated group ( $p < 0.01$ ) (Fig.8). The same pattern was maintained after 24 hours. AuNPs-CM reduced the inflammation (25 % inhibition) but insignificantly compared to vehicle ( $p > 0.05$ ) (Fig.8). The results obtained confirmed the structural changes induced in fatty acids by silver nanoparticles administration. It is known that arachidonic acid is metabolized by the sequential actions of prostaglandin synthase or by cyclooxygenase (COX) in prostaglandin E<sub>2</sub> (PGE<sub>2</sub>), prostacyclin (PGI<sub>2</sub>), prostaglandin D<sub>2</sub> (PGD<sub>2</sub>), and prostaglandin F<sub>2</sub> $\alpha$  (PGF<sub>2</sub> $\alpha$ ), known lipid mediators which act as autocrine and paracrine factors to maintain local homeostasis. PGE<sub>2</sub> is the most representative of PGs and acts

locally through binding of 1 or more of its 4 cognate receptors, termed E prostanoid receptor (EP)1–EP4.<sup>67</sup> PGE2 mediates augmentation of arterial dilatation and increases microvascular permeability, regulates the function of macrophages, dendritic cells (DCs) and T and B lymphocytes and secretion of proinflammatory cytokines.<sup>68</sup>

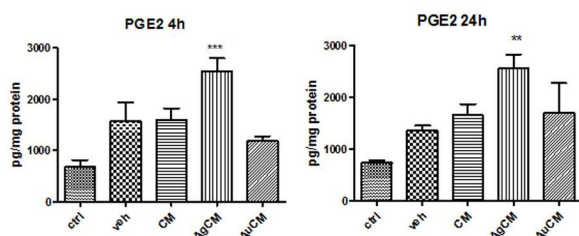


**Fig. 8** Prostaglandin E2 levels in paw tissue homogenates at 4 and 24 hours after induction of inflammation with carrageenan in animals pretreated with AuNPs-CM, AgNPs-CM and CM extract. AgNPs administered orally induced both at 4 and 24 hours after carrageenan injection increased of PGE2 secretion significantly compared to control, untreated group. Values are means±SD. Statistical analysis was done by a one-way ANOVA, with Tukey's multiple comparisons posttest (\*\*p<0.01; \*\*\*p<0.001).

Formation of eicosanoids via metabolism of arachidonic acid in inflammation and the important role of fatty acids in this pathology were the reasons that led us to investigate their spectroscopic properties.

## Conclusions

We provide here the proof of concept in employing Raman technique in interrogating the inflamed tissue from rats' models and demonstrated its applicability for monitoring the effect of nanoparticles administration in inflammation. Specifically, we have shown that AgNPs-CM induced inflammatory and cytotoxic effects on the skin tissue after oral administration, increased PGE2 levels and induced varying degrees of alteration of capillaries, cellularity, dermo-epidermal junction at conventional microscopy and TEM. The administration of AuNPs-CM

exhibited moderate anti-inflammatory effects while CM extract tends to reproduce the Raman spectrum of the normal skin tissue.

In conclusion, our results demonstrate that Raman spectroscopy can achieve high diagnosis accuracy and combined with microscopy is very powerful for imaging biological samples. The ultrastructural and histological changes in tissue in correlation with the biochemical results support the importance of Raman scanning for early detection of molecular changes *in vivo* and monitoring the efficiency of treatment. The promising results obtained create perspectives for further progress in early inflammatory conditions treatment based on natural extract-functionalized gold nanoparticles.

### Acknowledgment

This work was supported by the Ministry of Education, Research, Youth and Sports, Romania as a part of the research project no. 147/2012 PN-II-PT-PCCA-2011-3-1-0914. Monica Potara gratefully acknowledges the financial support of the Sectoral Operational Programme for Human Resources Development 2007-2013, co-financed by the European Social Fund, under the project POSDRU/159/1.5/S/137750 -“Doctoral and postdoctoral programs - support for increasing research competitiveness in the field of exact Sciences”. Special thanks are given to Dr. Ute Schmidt for assisting in cluster analysis.

### References

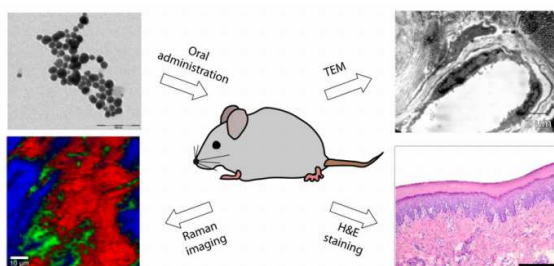
1. W. H. De Jong and P. J. A. Borm, *Int. J. Nanomedicine* 2008, **3**, 133–149.
2. M. C. Garnett and P. Kallinteri, *Occup. Med.*, 2006, **56**, 307–311.
3. A. Nel, T. Xia, L. Mädler, N. Li, *Science*, 2006, **311**, 622– 627.
4. C. S. Yah, *Biomed Res – India*, 2013, **24**, 400-413.
5. P. J. Caspers, G. W. Lucassen, G. J. Puppels, *Biophys J.*, 2003, **85**, 572–580.
6. L. Knudsen, C. K. Johansson, P. A. Philipsen, M. Gniadecka, H. C. Wulf, *J. Raman Spectrosc.*, 2002, **33**, 574–579.
7. S. Peterson, N. O. Faurskov, D. H. Christensen, H. G. M. Edwards, D. W. Farwell, R. David, P. Lambert, M. Gniadecka, H. C. Wulf, *J. Raman Spectrosc.*, 2003, **34**, 375–379.

8. S. Mert and M. Culha, *Appl. Spectrosc.*, 2014, **68**, 617-624
9. J. Choi, J. Choo, H. Chung, D. G. Gweon, J. Park, H. J. Kim, S. Park, C. H. Oh, *Biopolymers*, 2005, **77**, 264–272.
10. A. Nijssen, T. C. Bakker Schut, F. Heule, P. J. Caspers, D. P. Hayes, M. H. A. Neumann, G. J. Puppels, *J Invest Dermatol.*, 2002, **119**, 64–69.
11. T. R. Hata, T. A. Scholz, I. V. Ermakov, R. W. McClane, F. Khachik, W. Gellermann, L. K. Pershing, *J. Invest. Dermatol.*, 2000, **115**, 441–448.
12. G. Brevetti, G. Giugliano, L. Brevetti, W. R. Hiatt, *Circulation*, 2010, **122**, 1862–1875.
13. R. Medzhitov, *Nature*, 2008, **454**, 428-435.
14. Ren G, Zhao X, Zhang L, Zhang J, L'Huillier A, Ling W, Roberts A.I., Le A.D., Shi S, Shao C, Shi Y, *J. Immunol.*, 2010, **5**, 2321-8.
15. H. Tapiero, G. N. Ba, Couvreur P, K. D. Tew, *Biomed. Pharmacother.*, 2002, **56**, 215–222.
16. D. Pissuwan, T. Niidome, M. B. Cortie, *J. of Controlled Release*, 2011, **149**, 65-71.
17. G. E. Craig, S. D. Brown, D. A. Lamprou, D. Graham, N. J. Wheate, *Inorganic Chemistry*, 2012, **51**, 3490–3497.
18. R. T. Tom, V. Suryanarayanan, P. G. Reddy, S. Baskaran, and T. Pradeep, *Langmuir*, 2004, **20**, 1909–1914.
19. C. A. Simpson, J. Salleng K, D. E. Cliffler, and D. L. Feldheim, *Nanomedicine*, 2013, **9**, 257–263.
20. P. C. Chen, S. C. Mwakwari, A. K. Oyelere, *Nanotechnology*, 2008, **1**:45–66.
21. N. G. Bastus, E. Sanchez-Tillo, S. Pujals C. Farrera, M. J. Kogan, E. Giralt, A. Celada, J. Lloberas, V. Puentes, *Molecular Immunology*, 2009, **46**, 743–748.
22. H. J. Johnston, G. Hutchinson, F. M. Christensen, S. Peters, S. Hankin, V. Stone, *Crit. Rev. Toxicol.*, 2010, **40**, 328-346.
23. J. S. Kim, E. Kuk, K. N. Yu, J. H. Kim, S. J. Park, H. J. Lee, S. H. Kim, Y. K. Park, Y. H. Park, C. Y. Hwang, Y. K. Kim, Y. S. Lee, D. H. Jeong, M. H. Cho, 2007, **3**, 95–101.
24. B. Carlson, S. Hussain, A. Schrand, L. Braydich-Stolle, K. L. Hess, R. L. Jones and J. J. Schlager, *J. Phys. Chem.*, 2008, **112**, 13608-13619.

25. M. E. Shamberg, S. J. Oldenburg and N.A. Monteiro-Riviere, *Environ. Health Perspect.*, 2010, **118**, 407-413.
26. P. V. Asharani, M. P. Hande, S. Valiyaveetil, *BMC Cell Biol.*, 2009, **10**, 65.doi:10.1186/1471-2121-10-65.
27. E. J. Park, E. Bae, J. Yi, Y. Kim, K. Choi, S. H. Lee, J. Yoon, B. C. Lee and K. Park, *Environ. Toxicol. Pharmacol.* 2010, **30**, 162-168.
28. M. Ahamed, M. S. AlSalhi, M. K. Siddiqui, *Clinica Chimica Acta.*, 2010, **14**, 1841-1848.
29. M. Ahmad, M. Karns, M. Goodson, J. Rowe, S. M. Hussain, J. J. Schlager, Y. Hong, *Toxicol. Appl. Pharmacol.*, 2008, **233**, 404-410.
30. D. Mahl, C. Greulich, W. Meyer-Zaika, M. Koller, M. Epple, *J. Mater. Chem.*, 2010, **20**, 6176-6181.
31. A. H. Khan, M. A. K. Abdelhalim, A.S. Alhomida, M. S. Al-Ayed, *BioMed Research International*, 2013, <http://dx.doi.org/10.1155/2013/590730>
32. W. S. Cho, M. Cho, J. Jeong, M. Choi, H. Y. Cho, B. S. Han, S. H. Kim, H. O. Kim, Y. T. Lim, B. H. Chung, J. Jeong, *Toxicol. Appl. Pharmacol.*, 2009, **236**, 16-24.
33. K. U. Yilmaz, S. Ercisli, Y. Zengin M. Sengul, E. Y. Kafkas, *Food Chem.*, 2009, **114**, 408-412.
34. L. David, B. Moldovan, A. Vulcu, L. Olenic, M. Perde-Schrepler, E. Fischer-Fodor, A. Florea, M. Crisan, I. Chiorean, S. Clichici, G.A. Filip, *Colloids Surf. B Biointerfaces*, 2014, **1**, 122, 767-77.
35. M. M. Giusti, R. E. Wrolstad, in R. E. Wrolstad (Ed.), *Current Protocols in Food Analytical Chemistry*, Wiley, New York, 2001, Chapter F1.2
36. V. L. Singleton, R. Orthofer, R. M. Lamuela-Raventós, *Method. Enzymol.*, 1999, **299**, 152-178.
37. M. Crisan, L. David, B. Moldovan, A. Vulcu, S. Dreve, M. Schrepler-Perde, C. Tatomir, A. G. Filip, P. Bolfa, M. Achim, I. Chiorean, I. Kacso, C. Berghian Grosan, L. Olenic, *J. Mater. Chem. B*, 2013, **1**, 3152-3158.
38. C. R. Patil, A. R. Gadekar, P. N. Patel, A. Rambhade, S. J. Surana, M. H. Gaushal, *Homeopathy*, 2009, **98**, 88-91.

39. S A Maier *Plasmonics: Fundamentals and Applications* Springer, New York, 2007
40. T. Dieing and W. Ibach, *Software Requirements and Data Analysis in Confocal Raman Microscopy*, chapter in Confocal Raman microscopy, Springer series in optical sciences 158, Eds.T. Dieing, O. Hollricher, J. Toporski, Springer-Verlag, Berlin, Heidelberg, 2010.
41. J. Surmacki, J. Musial, R. Kordek and H. Abramczyk, *Molecular Cancer*, 2013, 12:48
42. D. I. Ellis, D. P. Cowcher, L. Ashton, S. O'Hagana and R. Goodacre, *Analyst*, 2013, 138, 3871-3884.
43. B. Brozek-Pluska, J. M. R. Kordek, E. Bailo, T. Dieing, H. Abramczyk, *Analyst* 2012,**137**, 3773-3780
44. L. Zhou and A. Nilsson, *J. Lipid Res.*, 2001, **42**, 1521–1542.
45. P. Benatti, G. Peluso, R. Nicolai and M. Calvani, *J. Am. Coll. Nutr.*, 2004, **23**, 281–302.
46. D. N. Granger, E. Senchenkova, J. Granger, New York: Morgan and Claypool Life Sciences; 2010.
47. L.A. Dykman and N. G. Khlebtsov, *Chem. Rev.*, 2014, **114**, 1258–1288.
48. M. Verdonck, N. Wald, J. Janssis, P. Yan, C. Meyer, A. Legat, D. E. Speiser, C. Desmedt, D. Larsimont, C. Sotirioud and E. Goormaghtigh, *Analyst*, 2013, **138**, 4083-4091
49. N. P. Seeram, R. Schutzki, A. Chandra, M. G. Nair, *J Agric Food Chem.*, 2002, **50**, 2519–23.
50. D. G. Kang, M. K. Moon, A. S. Lee, T. O. Kwon, J. S. Kim, H. S. Lee, *Biol. Pharm. Bull.*, 2007, **30**, 1796-1799.
51. H. F. Galley, N. R. Webster, *Br. J. Anaesth.*, 2004, **93**, 105-13.
52. J. Shaji, M. Lal, *Asian J. of Pharm. And Clin. Res.*, 2013, **6**, 3-12.
53. B. Semete, L. I. Booyesen, L. Kalombo, J. D. Venter, L. Katata, B. Ramalapa, J. A. Verschoor, H. Swai, *Toxicol. Appl. Pharmacol.*, 2010, **249**, 158-65.
54. C. Heneweer, J. P. Holland, V. Divilov, S. Carlin, J. S. Lewis, *J. Nucl. Med.*, 2011, **52**, 625–633.
55. M. Valko, C. J. Rhodes, J. Moncol, M. Izakovic, M. Mazur, *Chemico-Biological Interactions*, 2006, **160**, 1–40.

56. G. A. Fitzgerald and C. Patrono, *The New England Journal of Medicine*, 2001, **345**, 433–442.
57. P. J. W. Naude, A. D. Cromarty, E. Constance, R. V. Jansen, *Inflammapharmacology*, 2010, **18**, 33-39.
58. V. A. Chatpalliwar, A. A. Johrapurkar, M. M. Wanjari, R. R. Chakraborty, V. T. Kharkar. *Indian Drugs*, 2002, **39**, 543- 545.
59. J. Guay, K Bateman, R. Gordon, J. Mancini, D. Riendeau, *J. Biol. Chem.*, 2004, **279**, 24866–24872.
60. C. Sioutas, R. J. Delfino, M. Singh, *Environ. Health Res.*, 2005, **113**, 947-955.
61. L. Risom, P. Moller, S. Loft, *Mutat. Res.*, 2005, **592**, 119-137.
62. D. M. Brown, K. Donaldson, P. J. Borm, R. P. Schins, M. Dehnhardt, P. Gilmour, L. A. Jimenez, V. Stone, *J. Physiol. Lung Cell. Mol. Physiol.*, 2004, **286**, L344-L353.
63. B. Baroli, M.G. Ennas, F. Loffredo, M. Isola, R. Pinna, M. A. Lopez-Quintela, *J. Investig. Dermatol.* 2007, **127**, 1701–1712.
64. B. M. Rothen-Rutishauser, S. Schurch, B. Haenni, N. Kapp, P. Gehr: *Environ Sci Technol* 2006, **40**, 4353-4359.
65. M. T. Sorbara and S. E. Girardin, *Cell Res.*, 2011, **21**, 558e60.
66. D. Arnoult, F. Soares, I. Tattoli, S. E. Girardin, *EMBO Rep.*, 2011, 12:901e10.
67. C. E. Trebino, J. L. Stock, C. P. Gibbons, B. M. Naiman, T. S. Wachtmann, J. P. Umland, K. Pandher, J. M. Lapointe, S. Saha, M. L. Roach, D. Carter, B. A. Thomas, B. A. Durtschi, J. D. McNeish, J. E. Hambor, P. J. Jakobsson, T. J. Carty, J. R. Perez, L. P. Audoly, *Proc Natl Acad Sci U S A.*, 2003, **100**, 9044–9049.
68. E. Ricciotti, G. A. Fitzgerald, *Arterioscler Thromb Vasc Biol.* 2011, **31**, 986-1000.



The present study evaluated the potential of Raman spectroscopy as a technique capable to provide the diagnosis of skin inflammatory conditions and to differentiate the effect of treatments with silver and gold nanoparticles conjugated with natural extracts comparative with microscopy in experimental acute inflammation.